

Recent progresses in real-time local-basis implementation of time dependent density functional theory for electron–nucleus dynamics



Wei Ma^a, Jin Zhang^a, Lei Yan^a, Yang Jiao^a, Yi Gao^a, Sheng Meng^{a,b,*}

^a Beijing National Laboratory for Condensed Matter Physics, Institute of Physics, Chinese Academy of Sciences, Beijing 100190, China

^b Collaborative Innovation Center of Quantum Matter, Beijing, China

ARTICLE INFO

Article history:

Received 20 June 2015

Received in revised form 6 August 2015

Accepted 27 August 2015

Available online 11 September 2015

Keywords:

Time-dependent density functional theory

Ehrenfest dynamics

Excited state

Electron dynamics

ABSTRACT

We present an efficient real-time time-dependent density functional theory (TDDFT) method for large-scale accurate simulations of electron–nucleus dynamics, as implemented in the time dependent ab-initio package (TDAP). By employing a local basis-set presentation, we are able to simulate systems of large size (~500 atoms) and for long electronic propagation time (~300–500 fs) with less computation cost while maintaining relatively high accuracy. We show several quintessential examples, such as photoabsorption spectra of dye-sensitized TiO₂ nanowire, proton transfer coupled nonradiative relaxation of eumelanin constituents, electron injection and electron–hole recombination in dye solar cells, hole-transfer dynamics between MoS₂/WS₂ interlayer heterojunction, and solvent effects on electron dynamics. Our method is demonstrated to have superiority over available methods in dealing with interesting excited state characteristics of complex systems involving dynamics of electrons and atoms.

© 2015 Elsevier B.V. All rights reserved.

1. Introduction

The Born–Oppenheimer approximation [1–4], which assumes that the motion of the nuclei and electrons in a molecule or solid can be separated, is the most fundamental hypothesis in quantum physics and chemistry. However, in many situations, such as chemical or biological processes involving electron or proton transfer with significant tunneling or nonadiabatic effects, zero point motion in a chemical bond containing available energy smaller than that predicted by the potential depth, and the continuous rearrangement of a complex network of hydrogen bonds in water (inherently a quantum mechanical phenomenon), the Born–Oppenheimer approximation may often fail due to neglecting quantum mechanical electron–nucleus correlation effects. In such processes, the molecular system owns enough energy to explore the unusual regions of the configuration space, the adiabatic potential energy surface (PES) driving the time evolution of the system branches, and the nuclear wave packet splits among the manifolds of possible states.

The theoretical treatment of the time-dependent nonadiabatic phenomena is a formidable challenge at many levels, from the description of the excited states to the time propagation of the

corresponding physical properties. Given that the full quantum mechanical solution of such problems for large systems is out of question, several semi-classical approaches have been developed in the last half century to tackle the problem. They can be classified into three categories:

- (i) The wave packet propagation dynamics, such as the multi-configuration time-dependent Hartree (MCTDH) method [5]. The particular representation of the MCTDH wave function requires special techniques for generating an initial wave packet and for analyzing the propagated wave function. The full efficiency of the MCTDH method is only realized if the Hamiltonian can be written as a sum of products of one-dimensional operators. This method combines the efficiency of a mean-field method with the accuracy of the numerically exact solution, and performs especially well in systems containing many degrees of freedom (typically four to twelve). However, as in “conventional” nuclear wave packet propagation, PES are needed. It is of great difficulty to obtain and fit PES for large systems, thus the approach is very expensive to treat large systems. The largest system treated with MCTDH is the pyrazine molecule [5].
- (ii) The time evolution of density matrix, such as the mixed quantum–classical Liouville approaches [6–8]. In the mixed quantum–classical Liouville method, a partial Wigner

* Corresponding author at: Beijing National Laboratory for Condensed Matter Physics, Institute of Physics, Chinese Academy of Sciences, Beijing 100190, China. Tel.: +86 10 82649396.

E-mail address: smeng@iphy.ac.cn (S. Meng).

transform of the density operator, $\hat{\rho}$, is performed on the classical subspace, which maintains the operator form of the quantum part, and the classical part is described by functions of the classical Liouville phase-space variables, \mathbf{Q} and the momenta \mathbf{P} . The equations of motion involve a linearized approximation to an exponential time evolution operator in the classical subspace that keeps terms to the lowest order in \hbar . This approach describes well the dynamics of essentially nonlinear quantum systems for quite long times, but fails to describe quantum dynamics if a part of the Hamiltonian does not preserve irreducible subspaces of the symmetry group used for the mapping from the Hilbert space into the classical phase space.

- (iii) Semiclassical trajectory-based approaches, including Tully's trajectory surface hopping (TSH) [9–12], the Bohmian dynamics [13–15], the semiclassical Wentzel–Kramers–Brillouin (WKB) approximations [16–18], dephasing representation (DR) framework [19–21], Pechukas' path integrals method [22–23] and the mean-field nonadiabatic Ehrenfest dynamics [24–26]. Taking the quantum–classical mean-field Ehrenfest method as an example, it is commonly applied in treating the interaction between the quantum electronic motion and classical nuclear motion, where the electron wave function follows the time-dependent Schrödinger equation while the nuclei follow the classical Newton's law. These trajectory-based approaches can run on the fly without the need to parameterize the PES, and can handle large molecules in the full configuration space without huge computational efforts. Usually this is done together with the assumption that the interactions between the nuclei follow some empirical potential models. However, there are some problems associated with these empirical models: (a) the excited state PES, which are different from ground state PES, are missing in these simulations, thus the electronic properties in excited states cannot be addressed adequately in empirical models and (b) the forces of the system, which are subject to the details of nonlocal interactions and geometry configurations of the system, may not be accurate enough, thus the time scales obtained therein are questionable.

Here we propose a real-time ab initio approach for electron–nucleus dynamic simulations beyond the Born–Oppenheimer approximation, which follows Ehrenfest dynamics and represents a mean-field theory of the mixed quantum–classical system, with forces on the nuclei are averaged over many possible adiabatic electronic states induced by nuclei motion [27–32]. The method has been implemented successfully in the time-dependent ab initio package (TDAP) within the framework of density functional theory (DFT) and time-dependent DFT (TDDFT). We use local atomic basis sets and real-time propagation of wave functions for solving the time-dependent Kohn–Sham (TDKS) equations, which endows our approach several advantages over available conventional methods:

- (i) The adoption of overwhelmingly efficient atomic orbital basis sets, which are small in size and fast in performance, enables simulations of either periodic system or a finite-sized supercell with large vacuum space without heavy calculation cost while maintaining relatively high accuracy.
- (ii) Real time excited state trajectories are achieved with many-electron density self-consistently propagating at every electronic and nuclear steps and forces are calculated from mean-field theory, offering a direct microscopic picture on the ultrafast dynamics of electrons and nuclei upon photo-excitation.

- (iii) Relatively high efficiency for parallelization can be achieved because the occupied molecular orbitals are propagated independently at a time and can be distributed evenly over several processors with little mutual communication.
- (iv) Photo-absorption spectra and polarizability of the computed systems can be calculated within the same scheme. Nonlinear effects can also be treated precisely [33,34].

Our approach behaves well in treating dynamic processes such as interface electron injection, electron–hole recombination and charge transfer induced chemical reactions, where a single path dominates in the reaction dynamics. However, in mean-field regime, Ehrenfest dynamics describes nuclear paths using a single averaged trajectory even when the nuclear wavefunction has broken up into distinct parts. Therefore, the approach fails to deal with situations where multiple paths are involved in the excited states, especially when state-specific nuclear trajectories are of interest [35]. It also lacks a detailed balance for quantum electronic states [36]. We limit our studies to the former cases and especially look into the early stages of excited state dynamics. When there is branching, our approach can address issues related to the mechanisms leading to the branch or decay. For alternative strategies, when trajectories other than Ehrenfest dynamics are needed to model nonadiabatic processes, the readers are referred to methods which explicitly include electronic transitions such as trajectory surface hopping [9–12,37].

2. Methodology

2.1. Time-dependent Kohn–Sham equations for coupled electron–nucleus motion

Under the TDDFT formalism, the coupled electron–nucleus (or electron–ion) system follows the general time-dependent Schrödinger's equation:

$$i\hbar \frac{\partial \Psi(\{r_j\}, \{R_j\}, t)}{\partial t} = H_{\text{tot}}(\{r_j\}, \{R_j\}, t) \Psi(\{r_j\}, \{R_j\}, t), \quad (1)$$

where r_j and R_j are the positions of the j th electron and J th nucleus, respectively. H_{tot} denotes the time-dependent Hamiltonian of the multicomponent system written as:

$$H_{\text{tot}} = -\sum_j \frac{\hbar^2}{2m} \nabla_j^2 - \sum_J \frac{\hbar^2}{2M} \nabla_J^2 + \frac{1}{2} \sum_{i \neq j} \frac{e^2}{|r_i - r_j|} + \frac{1}{2} \sum_{I \neq J} \frac{Z_I Z_J}{|R_I - R_J|} - \sum_{jJ} \frac{eZ_J}{|r_j - R_J|} + U_{\text{ext}}(\{r_j\}, \{R_j\}, t) \quad (2)$$

According to the Rung–Gross theorem [38], the external potentials for the electrons v_s and ions V_s^J are determined only by their respective densities,

$$v_s[\rho](r, t) = v_{\text{ext}}(r, t) - \sum_I \frac{Z_I \rho_I(R, t)}{|r - R|} dR + \int \frac{\rho(r', t)}{|r - r'|} dr' + v_{\text{xc}}[\rho](r, t), \quad (3)$$

$$V_s^J[\rho](R, t) = V_{\text{ext}}^J(R, t) - Z_J \int \frac{\rho(r, t)}{|R - r|} dr + Z_J \sum_I \frac{Z_I \rho_I(R', t)}{|R - R'|} dR' + V_{\text{xc}}^J[\rho](R, t), \quad (4)$$

where $\rho(r, t) = \sum_j |\phi_j(r, t)|^2$, $\rho_j(R, t) = \sum_j |\psi_j(R, t)|^2$.

As the nuclei are much heavier than electrons by at least three orders of magnitude, we define the nuclear positions following the Newton's second law:

$$M_J \frac{d^2 R_J(t)}{dt^2} = -\nabla_{R_J} \left[V_{\text{ext}}^J(R_J, t) - \int \frac{Z_J \rho(r, t)}{|R_J - r|} dr + \sum_{I \neq J} \frac{Z_I Z_J}{|R_J - R_I|} \right]. \quad (5)$$

Note that here we ignore the negligible nucleus–nucleus exchange–correlation function and assume that the ionic density has a sharp distribution $\rho_j(R, t) = \delta(R - R_j(t))$. The motion of electrons follow the TDKS equations where,

$$i\hbar \frac{\partial \phi_j(r, t)}{\partial t} = \left[-\frac{\hbar^2}{2m} \nabla_r^2 + v_{\text{ext}}(r, t) + \int \frac{\rho(r', t)}{|r - r'|} dr' - \sum_i \frac{Z_j}{|r - R_j|} + v_{\text{xc}}[\rho](r, t) \right] \phi_j(r, t). \quad (6)$$

Eqs. (5) and (6) represent the time-dependent coupled electron–nucleus motion. The TDKS equations of electrons and the Newtonian motion of nuclei are solved simultaneously, with nuclear forces along the classical trajectory are evaluated through the Ehrenfest theorem.

2.2. Propagation and parameters

With the present scheme, we can perform ab initio molecular dynamics (MD) for coupled electron–nucleus systems with the motion of nuclei following the Newtonian dynamics while electrons following the TDKS dynamics. The nuclei velocities and positions are calculated using Verlet algorithm at each time step. When the initial conditions are chosen, the electronic subsystem may populate any state, ground or excited, and is coupled nonadiabatically with the motion of nuclei.

Fig. 1 shows the flowchart of electron–nucleus molecular dynamics simulations. Initially, a self-consistent diagonalization is performed for a given nuclei configuration $\{\mathbf{R}(0)\}$ at the initial temperature (usually set as 350 K), which is determined by the ionic velocities $\{\mathbf{v}(0)\}$. The resulting Kohn–Sham (KS) eigenstates are $\{\phi_j(0)\}$, where j is the index of the occupied states. By switching the occupation of the corresponding KS states involved in the photo-excitation, we are able to model the initial photo-excited state. Note that the self-consistent electron density includes only contributions from an updated set of occupied states, thus the contribution of excited state amounts to a constrained DFT calculation at $t = 0$. In principle, partial occupation of several states is allowed here.

At $t > 0$, the time evolution of $\{\phi_j(t)\}$ is realized by multiplying the time propagator at the n th step ($t_n = n\Delta t$). We can approximate the exponential propagator to be the Crank–Nicholson operator [39],

$$U = \exp(-i\hbar H\Delta t) = (1 - i\hbar H\Delta t/2)/(1 + i\hbar H\Delta t/2). \quad (7)$$

A higher order Crank–Nicholson operator can also be used at the cost of computation time. The time step for real time propagation of Kohn–Sham wave functions in our simulations is 0.02419 fs.

As shown in Fig. 1, a self-consistent operation is performed before the new wave function can be accepted, which assures time reversal symmetry and is critical to the stability of long time simulations. It should be noted that the self-consistent loop of the excite state here has no bearing on the ground state self-consistency because no diagonalization of the Hamiltonian matrix is performed. Therefore, the new wave function $\{\phi_j(t_{n+1})\}$ are not eigenstates of the updated Hamiltonian $H(t_{n+1})$, however, their density reproduces the same potential by which they are generated. Within this scheme, the total energy is well conserved to within 10^{-4} eV/fs, which is proved to be accurate enough to produce negligible differences in energy levels evolution and electron–nucleus dynamics. We employed the Pulay mixing scheme for self-consistent calculation and only occupied KS orbitals are needed for time evolution. The forces acting on the nuclei can be calculated according to the Ehrenfest theorem once the self-consistent potential is obtained.

After evaluating all the force terms on each ion, we can then calculate the new ionic positions and velocities $\{\mathbf{R}_{n+1}\}$ and $\{\mathbf{v}_{n+1}\}$ at time $t_{n+1} = (n+1)\Delta t$ based on the Verlet algorithm. The off-diagonal Hamiltonian matrix element E_{ij} is monitored in order to assess the applicability of Hellmann–Feynman-like forces in the excited-state TDDFT simulations. When E_{ij} ($i \neq j$) is comparable to typical energy separation $\Delta E = E_{ii} - E_{jj}$, states i and j have high

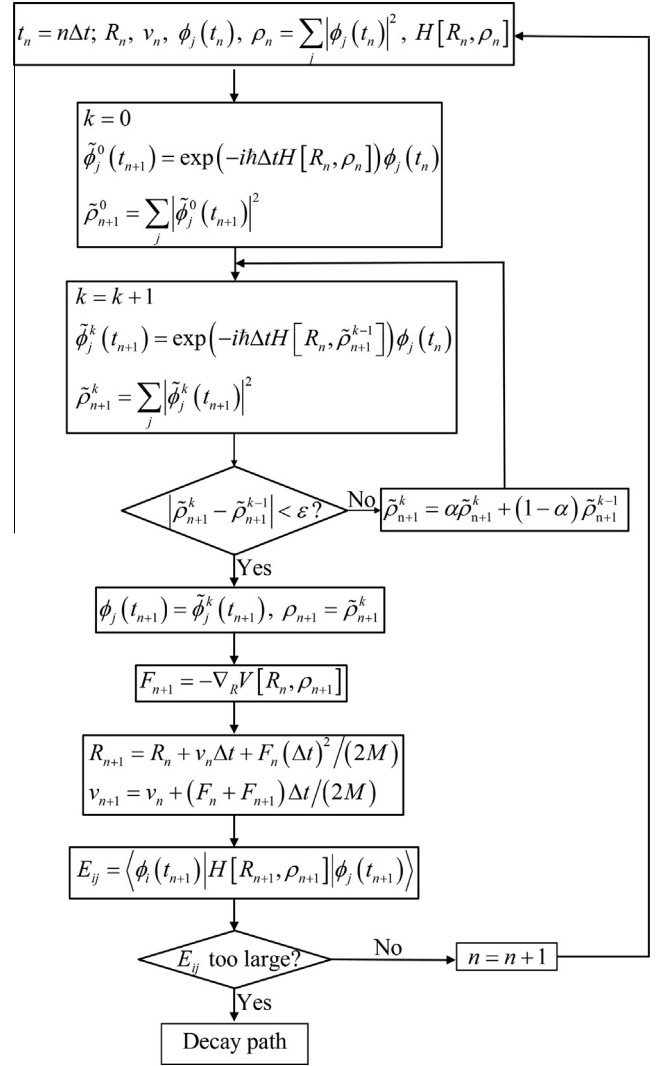


Fig. 1. The schematic flowchart of the real-time excited state MD simulations. The iterations over the index k describe the self-consistency loop. E_{ij} in the second rhombus box is the off diagonal Hamiltonian matrix element ($i \neq j$).

tendency of state mixing and high recombination probability between the two states, which also indicates the failure of the nonadiabatic TDDFT simulations.

2.3. Modeling interface electron injection

Ultrafast electron and hole dynamics upon light excitation in molecular and semiconducting systems are key processes in many types of photovoltaic and optoelectronic devices. These processes are usually coupled to local or periodic atomic vibrations during carrier transport and relaxation processes, so both the electronic and nuclear degrees of freedom need to be considered. To simulate the interface electron–nucleus dynamics, we take the sensitizer/semiconductor interface in the prototype dye-sensitized solar cells (DSC) as an example. At time $t = 0$, an electron is promoted from the highest occupied molecular orbital (HOMO) of the sensitizer to its lowest unoccupied molecular orbital (LUMO), representing the first excited state that a pair of electron and hole is generated upon photoabsorption. Electronic state diagonalization is performed at this first step after the occupation switch. Then we let the coupled electron–nucleus system evolve in real time. The initial ionic temperature is set to 350 K. By monitoring the fraction

of photo-excited electrons $\chi(e)$ distributed in the sensitizer and semiconductor substrate, we can obtain the lifetime of electron injection by an exponential fitting to $\chi(e)$ as a function of time after light excitation.

2.4. Modeling electron–hole recombination

Electron–hole recombination is an essential and important energy loss process in the light-to-electricity energy conversion. High efficiency energy conversion must require minimal electron–hole recombination losses. To model electron–hole recombination process, we also take the dye/semiconductor interface in DSC as an illustrative example. In contrast to electron injection simulations where the HOMO and LUMO of the sensitizer are switched at $t = 0$, the occupation of the conduction band minimum (CBM) of the TiO₂ semiconductor and the HOMO of the sensitizer are switched, representing the initial state where electrons are mainly distributed on TiO₂ and the holes stay in the chromophore. Electronic state diagonalization is performed at this first step after the occupation switch. Then we let the coupled electron–ion system evolve in real time. Different kinds of initial excitation states are sampled, which correspond to excitations from HOMO of the dye to different energy levels of TiO₂ conduction bands (CB). Note that, all these final states are low energy states of TiO₂ and do not represent substantial physical differences. By averaging these trajectories, we obtain the timescale for recombination dynamics. As the electron–hole recombination process is extremely slow (with a lifetime in the range of picosecond to nanosecond), ideally the recombination yield would be linearly decaying as a result of statistical average of many trajectories. However, we have calculated only a few trajectories due to the limit of high computational cost. Therefore, some recombination process shows alternatively large fluctuations around the linearly decaying behavior.

2.5. Comparisons to trajectory surface hopping

The fewest-switch trajectory surface hopping methods [9–12] developed by Tully and others is a powerful approach for electron dynamics simulations. TSH is based on the hypothesis that the time evolution of a wave packet through a potential-energy branching region can be approximated by an ensemble of independent semi-classical trajectories stochastically distributed among the branched surfaces. Electronic redistribution is achieved by allowing hops between surfaces according to some probability distribution. TSH method is a mixed quantum–classical treatment of the molecular evolution, with the adiabatic dynamics of the nuclei propagating classically on a single Born–Oppenheimer surface at any given time, whereas the branching of the population due to nonadiabatic effects is introduced by a stochastic algorithm allowing the exchange of electronic state during the dynamic propagation [9]. This partition gives rise to a semi-classical trajectory always propagating on a single surface, but with the possibility of exchanging the surfaces. The approximation makes TSH successful in treating nonadiabatic dynamics of large systems with a low computation cost [40,41]. However, there are some problems accompanied: (a) The free flow of energy among degrees of freedom in the classical trajectories may lead to inconsistent treatment of zero-point energy. (b) The local character does not allow the treatment of tunneling effects. (c) The coherence between states is usually wrong because of the independent trajectory approach. (d) When on-the-fly approaches are employed, the computational costs are often too high to achieve proper statistical convergence in the number of trajectories or to propagate the trajectories for longer than a few picoseconds [42].

To obtain a direct view of the differences between the present TDAP method with other approaches, we simulate electron

injection dynamics from the sensitizers N1 and N2 to the nanocrystal TiO₂ substrate using TDAP method and Tully's trajectory surface hopping method, as shown in Fig. 2.

From Fig. 2a, we found that excited electrons completely inject into the CB of the TiO₂ substrate within a time scale of 162 fs for N1 and 146 fs for N2, while holes are kept stable and confined within the dye molecule, based on state-of-the-art real-time excited state TDDFT simulations [43]. Fig. 2b shows that the electron injection exhibits an ultrafast dynamics with a lifetime of 11.83 fs for N1 and 11.53 fs for N2 calculated from TSH method. The timescale obtained from TSH method is ten times faster than the present TDDFT approach. This is mainly resulted from the high LUMO level of the sensitizers above the TiO₂ conduction band edge, leading to high density of states of TiO₂ substrate near dye LUMO, thus giving rise to large probability of electron hopping in TSH.

Even greater differences between TDAP and TSH approaches come from the simulation of electron–hole recombination dynamics. Fig. 3 shows the dynamic electron back transfer from the TiO₂ to the sensitizers N1 and N2 in the initial process of electron–hole recombination. Immediately after promoting an electron to the CB of TiO₂, the electron has a dominant distribution in the CB of TiO₂. The energy difference between the CB of TiO₂ and the HOMO of the dye drives electron transfer from TiO₂ back to the sensitizer. It is obvious that the recombination rates for both dyes exhibit a good linear decaying behavior and the longer molecule N2 clearly shows a slower decaying behavior. The timescale of the recombination process, 6 ps for N1 and 23 ps for N2, are obtained by extending the linear curve to the intersection where the electron is completely transferred to the dye (Fig. 3a and b). This is in agreement with experimental observations that the recombination rate is 5 times slower in N2 sensitized devices than that for N1 measured by laser photolysis [44]. In contrast, we note that time-domain surface hopping approach based on ground state trajectories produces too fast recombination for N1 (1.57 ps) and N2 (1.43 ps) (see Fig. 3c and d). Dyes N1 and N2 exhibit very similar electron–hole recombination dynamics at dye/TiO₂ interface in the TSH approach. Thus the surface hopping results cannot account for the finite difference in recombination timescales between N1 and N2 sensitized devices, and are therefore at discrepancy with experiment [44].

2.6. Parallelization

In the real-time TDDFT scheme, the single-electron Kohn–Sham wave functions are evolved separately, which makes the scheme extremely efficient in parallel computation. Meanwhile, only occupied states contribute to the electronic density, therefore, we just need to consider the wave functions of occupied states for computation.

We have implemented the current approach in the popular first-principles software SIESTA, which is used to compute the initial wave functions and the Hamiltonian matrix at each time step [27]. SIESTA uses atomic orbitals as a basis set involving a set of localized numerical atomic orbitals, which are spatially confined and being strictly zero beyond a certain distance from the corresponding nucleus. Therefore, the density, Hamiltonian and overlap matrices are sparse matrices. Secondly, the Hartree and exchange–correlation potentials and their matrix elements are calculated via projecting the electron wave functions and density onto a real-space grid. Besides the standard Rayleigh–Ritz eigenstate method, it allows the use of linear combinations of localized orbitals (valence-bond or Wannier-like functions), making the computer time and memory can scale linearly with the number of atoms. Thirdly, we employ the ScaLAPACK library for linear algebra computation, and column splitting for storage and matrix calculations, which ensures even distribution of Kohn–Sham orbitals over

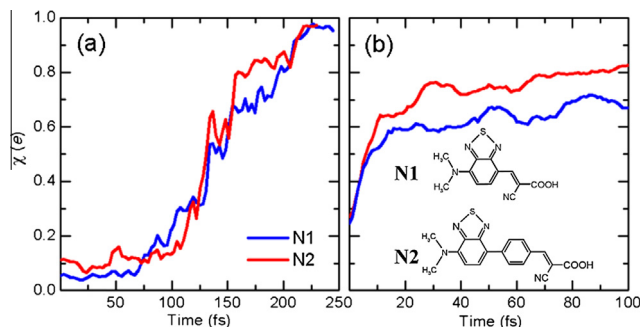


Fig. 2. Electron injection dynamics from the sensitizer to TiO_2 substrate simulated by (a) TDAP approach, (b) TSH method. The inset in figure (b) shows the chemical structure of the sensitizers, N1 and N2, in the simulations.

processors with little mutual communication. Consequently, simulations with several hundred atoms are feasible with modest workstations.

Based on the parallelization method mentioned above, the TDAP approach assigns the independently-evolving electronic wave functions evenly to each processor, and reduces data transmission. The dominating computation costs are calculations of the Hamiltonian and its evolution operators. After parallelizing the computation for evolution operators, the computing speed can be improved by eight times for a typical system. Fig. 4 shows the parallel computing efficiency we tested. The test system contains 124 atoms with 1580 basis sets and 320 real-time time-dependent single-electron Kohn–Sham wave functions. The relatively high parallel efficiency makes it possible for us to efficiently investigate the excited state dynamics of large and complex systems.

3. Some recent examples towards realistic applications

3.1. Photoabsorption spectra of dye-sensitized TiO_2 nanowire

We have employed the real-time local-basis TDDFT approach to investigate the electron–nucleus dynamics in a few prototypical model systems for important applications such as photovoltaics and photocatalysis. First, we use the present method to calculate the photoabsorption properties of dye/semiconductor combined system to investigate the sensitizing effect and electronic couplings between the dye molecule and the semiconductor substrate. To calculate the optical properties of system under investigation, we monitor the dynamic evolution of the electric dipole moment of the system after perturbation by an external field based on real-time TDDFT simulations. The intensity of optical absorption can be expressed as:

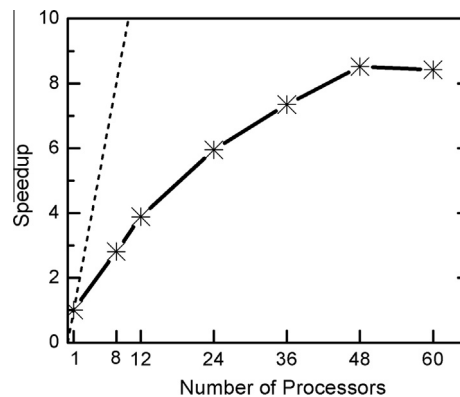


Fig. 4. Parallel computing efficiency of TDAP. The test system contains 124 atoms with 1580 basis sets and 320 real-time evolving time-dependent single-electron wave functions.

$$S(\omega) = \frac{2m}{\pi e^2 \hbar} \omega \ln \alpha(\omega), \quad (8)$$

where $\alpha(\omega)$ is the polarizability $\alpha(\omega) = d(\omega)/E(\omega)$ and $d(\omega)$ is the dipole moment of the system. At $t = 0$, we introduce an instantaneous perturbation electric field, which is,

$$E(t) = \bar{E}\theta(-t). \quad (9)$$

After Fourier transform of Eq. (9) in frequency space, it become

$$E(\omega) = \bar{E}/(i\omega). \quad (10)$$

Substituting Eq. (10) in Eq. (8), we have

$$S(\omega) = \frac{2m\omega^2}{\pi e^2 \hbar \bar{E}} \text{Re} \int_0^\infty dt e^{i\omega t - \delta t} d(t), \quad (11)$$

which should satisfy the f-sum rule:

$$\hbar \int_0^\infty d\omega S(\omega) = \sum_i f_i = N_e. \quad (12)$$

Here, f_i is the intensity of optical response, N_e is the number of electrons. From Eq. (8), we can calculate the absorption spectra of the system by simply keeping track of the dipole moment $d(t)$ in real time after the instantaneous field perturbation.

Fig. 5 shows the optical properties of the cyanidin/ TiO_2 nanowire calculated using TDAP [29]. A finite segment of the $[1\bar{1}1]$ nanowire of anatase phase TiO_2 is adopted, which is terminated by OH and H at the two ends along its axis, resulting in a structure consisting of $20(\text{TiO}_2) \cdot 2(\text{H}_2\text{O})$. We choose the base structure of cyanin without the sugar group, the cyanidin (Cya) molecule as the sensitizer adsorbed onto TiO_2 nanowire (inset of Fig. 5). For

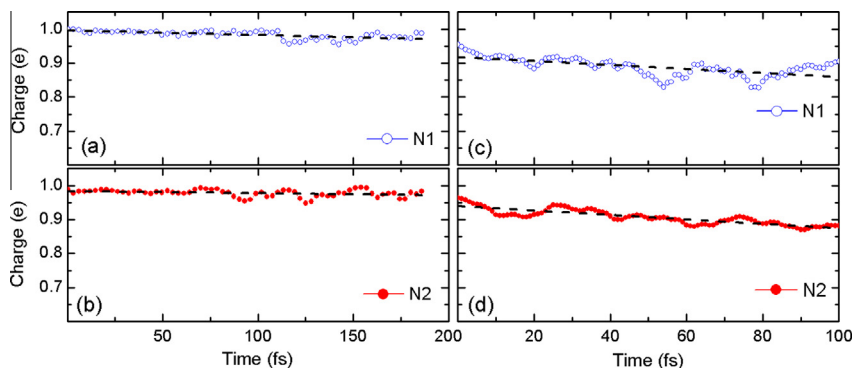


Fig. 3. Electron recombination dynamics from TiO_2 to the sensitizer simulated by the (a and b) TDAP and (c and d) TSH method.

comparison, absorption spectra of the bare TiO₂ nanowire (red¹ dashed line in Fig. 5) and free Cya molecules (green dotted line in Fig. 5) are also calculated. Cya exhibits two major absorption bands at 520 and 410 nm, respectively, agreeing well with the experiment results (520 nm) [45]. When adsorbing on the TiO₂ nanowire, these two peaks are red-shifted to 650 and 480 nm with notably enhanced intensity, which originates from the interfacial Ti–O coupling between the molecule and the nanowire. The bare TiO₂ nanowire shows no absorption in the region beyond 400 nm, consistent with its large band gap \sim 3.2 eV. The dye sensitizer greatly increases the absorption of TiO₂ nanowire in the visible range, which dominates the terrestrial solar spectrum. In experiment, cyanin on TiO₂ nanoparticles show absorption peaks at 532 nm. The differences in absorption spectra of dye-sensitized TiO₂ may be assigned to the versatility of dye adsorption configurations and different TiO₂ structures (nanowires in the calculation versus nanoparticles in experiment). The excellent agreement with the experiment absorption spectra of free Cya dye demonstrates that our method is efficient and accurate in calculating optical properties, opening up a new way to precisely calculate photoabsorption spectra of large systems.

3.2. Excited state bond breaking/reforming in eumelanin constituents

Melanin is believed to be crucial for defense against UV radiation damage [46,47] via a unique set of optical properties including broadband absorption [48], extremely low scattering (<6%) and emission (<0.1%) [49], ultrafast relaxation dynamics [50–51] and ability to transfer X-ray energy into chemical energy [52]. By using real time TDDFT calculations, we are able to investigate nonradiative relaxation processes in eumelanin model constituents including its indole building blocks (indolequinone (IQ), quinone-methide (MQ), quinone-imine (NQ)) as monomer, and in oligomers such as dimers and trimers [28].

Our simulations show that after photoexcitation, MQ quickly relaxes into NQ structure by transferring an H atom from O1 to O2 site, as shown in Fig. 6. The proton transfer is an activated process. The potential energy is monitored during the relaxation dynamics simulation, which shows a barrier of <0.2 eV for proton transfer. Our results demonstrate that this process occurs when the initial temperature is $T_0 = 300$ K, but does not happen at $T_0 = 0$ K. During proton transfer, the electron density of the HOMO shows a concerted transition of π -bond pattern from MQ to NQ, involving double bond breaking and reforming (Fig. 6). The transition from MQ to NQ can have momentary setbacks, and the molecule relaxes to its initial state with a broken C7–C8 bond if the H is not successfully transferred (as at $\sim t = 103$ fs). At $t = 114$ fs, the proton is triumphantly transferred, the bonding in the molecule evolves into a new pattern and the potential energy is lowered by ~ 0.1 eV ($t = 118$ fs). From the electron density distributions (inset of Fig. 6), we observe that the H transfer process is forcefully coupled with electron redistribution around the neighboring O sites, indicating it is actually H atom transfer. Therefore, the eumelanin molecules can transform photon energy into thermal energy by proton transfer in a remarkably short timescale of ~ 100 fs. This agrees well with the former photochemistry studies that excited-state intramolecular proton transfer is mostly H atom transfer with intrinsic electron–proton couplings [53].

3.3. Photoelectron injection into semiconductors

In photovoltaic devices such as DSC, efficient photoelectron injection enables high photon-to-electricity conversion efficiency.

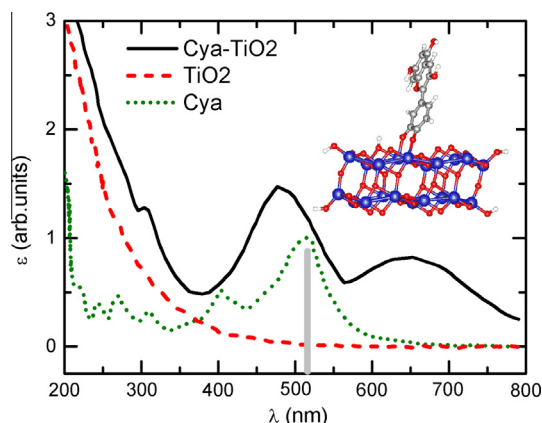


Fig. 5. Optical absorption spectra of a finite segment of TiO₂ nanowire with (solid) and without (dashed) sensitizing dye molecules. The calculated spectrum for a free cyanidin molecule is also shown (dotted), together with the experimental peak position (vertical bar). Inset is the chemical structure of cyanidin sensitized TiO₂.

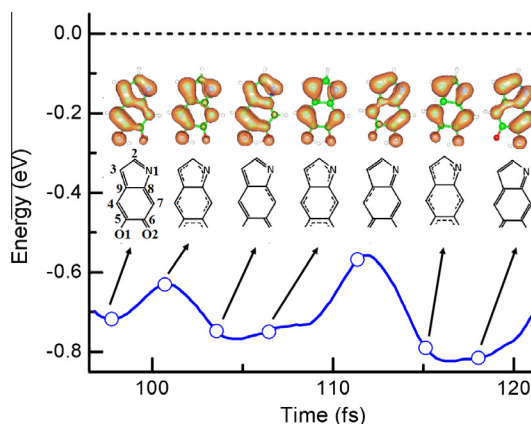


Fig. 6. Concerted electron–proton motion. The evolution of total energy (black dashed line) and potential energy (blue line) of quinone-methide after photoexcitation is shown as a function of time. Insets are snapshots of the HOMO electron density (at contour level $0.02 \text{ e}/\text{\AA}^3$) and corresponding bonding diagrams, which show the evolution of π -bond patterns during proton transfer. (For interpretation of the references to colour in this figure legend, the reader is referred to the web version of this article.)

Understanding the mechanism of ultrafast electron injection in photovoltaic devices and factors limiting the photoelectron injection efficiency are of great importance to optimize device performance. Here, we have calculated the injection rates of two dyes D404 (with cyanoacrylic acid anchor moiety) and SY404 (with acyloin anchor group) sharing the same donor using real-time excited state TDDFT simulations to directly investigate the influence of anchoring groups in electron injection dynamics [54]. From Fig. 7, at time $t = 0$, electrons have a dominant distribution on the sensitizers, then the energy difference between the molecular LUMO level and the TiO₂ conduction band minimum drives electrons to efficiently inject into the substrate with a lifetime of 33 fs for dye SY404 and 60 fs for dye D404. Apparently, SY404 dye with acyloin anchor possesses a faster electron injection dynamics due to the stronger electronic coupling strength with the TiO₂ substrate.

3.4. Influence of molecular structure on electron–hole recombination

Even efficient injection is guaranteed in photovoltaics, if injected electrons on the TiO₂ conduction band do not rapidly

¹ For interpretation of color in Fig. 5, the reader is referred to the web version of this article.

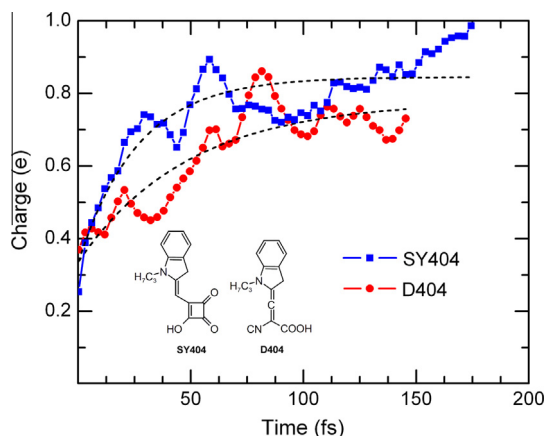


Fig. 7. The fraction of photo-excited electrons distributed on TiO_2 substrate as a function of time after photoexcitation of dyes SY404 and D404 with different anchor groups using real-time TDDFT simulation. The insets are chemical structures of dyes SY404 and D404. Dashed lines show exponential fittings of the injection dynamics.

transport to the conducting contact, they will easily lose energy by recombining with holes in the electrolyte and the oxidized sensitizers, hence limiting the attainable energy conversion efficiency. Therefore, retarding the interface charge recombination is beneficial for improving the device's energy conversion efficiency. Haid et al. have decreased electron–hole recombination rates by about 5 times through inserting a phenyl ring between the benzothiadiazole (BTDA) bridging unit and the cyanoacrylic acid acceptor [44]. Understanding how the slight structural modifications dramatically affect the charge recombination is crucial for DSC optimization. We have simulated the recombination process at simplified model dyes N1 (N2)/ TiO_2 interface using real-time excited state TDDFT, and found that the five times changing in recombination rate mainly comes from the longer back electron transfer distance of the inserted dye using quantum chemical simulations [43]. As shown in Fig. 8a, the insertion of an additional phenyl ring close to the anchoring group significantly slows down the electron–hole recombination rate by about four times (23 ps vs. 6 ps).

Besides longer recombination distance, many people think that structural twisting of donor- π -acceptor dye can break down the π -conjugation between the donor and acceptor and thus block electron back transfer to the sensitizer from the charge separated state. We have also investigated the influence of structural twisting on dye/ TiO_2 interface electron–hole recombination by calculating the recombination timescale of two isomer dyes N3 and N4 adsorbed on TiO_2 anatase (101) surface based on real time excited state TDDFT. [54] Fig. 8b shows the evolution of electrons transferred back from the TiO_2 conduction band to the sensitizers. Two insets are the chemical structures of dyes N3 and N4. N3 and N4 share same compositions but have $\sim 30^\circ$ difference in dihedral angles between the donor moiety and bridging unit. Obviously, dyes N3 and N4 exhibit similar recombination dynamics and the planar dye N4 even shows a slower recombination dynamics. Therefore, structural torsion of organic dyes hardly affects the recombination process at dye/ TiO_2 interface.

3.5. Solvent effects in interface electronic dynamics

We apply the present method to a more complex system, which contains dye sensitized nanocrystalline TiO_2 in explicit solvent environment. Highly effective DSCs are usually synthesized and characterized in a solution environment. Solvent molecules can influence both the conformation and electronic structure of the

adsorbate/ TiO_2 interface, altering the interfacial charge transfer process in nano-composites and limiting the overall efficiency of the photovoltaic devices. Based on real-time excited state dynamics simulations of electron transfer processes at the dye/semiconductor/electrolyte heterointerface, we are able to gain full atomistic insights into the solvation effects in the molecule–solid–liquid nano-complex at room temperature.

Fig. 9(a) shows the atomic structure of the simulation cell, containing a 96-atom TiO_2 slab, an organic dye molecule M0, and 18 acetonitrile molecules (equivalent to a density $\rho \sim 786$ mg/mL). Fig. 9(b) shows the recombination dynamics of electrons in TiO_2 CBM and holes in dye HOMO with and without solvent. Immediately after promoting an electron to the CB of TiO_2 , the electrons have a small fraction of distribution in the sensitizer and solvents. The energy difference between the CB of the TiO_2 and the HOMO of the dye drives electron transfer from TiO_2 to the sensitizer in an approximately linear increasing trend. The vacuum system clearly undergoes a faster recombination dynamics with lifetime of ~ 23 ps, while recombination lifetime in the solvation system is much longer (>200 ps). This significant difference confirms that, the presence of strong polar solvents such as acetonitrile drastically slows down electron–hole recombination at M0/ TiO_2 /acetonitrile heterointerface by about ten times! Interestingly, we find that solvent molecules can adsorb on the TiO_2 substrate, forming an interface dielectric layer at dye/ TiO_2 heterointerface, thus remarkably blocking the recombination of injected electrons with holes in the electrolyte by preventing direct contact of oxidized species in the electrolyte with the TiO_2 anatase (101) surface. The ten times difference in recombination rates with and without organic solvents provides a natural way to explain the high efficiency ($>10\%$) of dye solar cell devices fabricated with organic solvents.

3.6. Interface electronic dynamics between MoS_2 / WS_2 interlayer

Interestingly, we can also monitor the electronic dynamics at the interface of different semiconductor materials. We use MoS_2 / WS_2 heterojunction as an example to show how this approach works. Two dimensional (2D) layered materials including graphene [55,56], hexagonal-boron nitride and transition-metal dichalcogenides (MX_2) have opened up a new avenue for van der Waals heterostructures. MX_2 heterostructures are particularly interesting for optoelectronic and photovoltaic applications, because 2D MX_2 monolayers display an optimized band gap for the near-infrared to visible spectral range absorption [57]. Many MX_2 heterostructures can form type II semiconductor heterojunctions [58], which facilitate efficient electron–hole separation for light detection and light harvesting. Stacking structure of MoS_2 – WS_2 heterostructure has been presented in Fig. 10 (a) and (b), where the height between the two layers is 6.3 Å. Due to the similar lattices of the two layers, lattice mismatch can be neglected in our model. Projected density of states (PDOS) is given in Fig. 10(c). It is clear that the conduction band minimum of MoS_2 layer is lower than that of WS_2 while the valence band maximum of MoS_2 layer is higher than that of WS_2 by ~ 0.5 eV.

We then analyze the ultrafast charge transfer process. At $t = 0$ fs, one electron is promoted from MoS_2 VBM to its CBM to imitate the first photo-excited state. Then the electron–ion coupled system begins to evolve in real time using a time step of 0.02419 fs. Initially, holes have a dominated distribution on WS_2 layer, which is presented in Fig. 10(d). The energy barrier between CBM of MoS_2 and WS_2 keeps the excited electron stay on MoS_2 layer (not shown). In the meantime, energy difference between VBM of MoS_2 and WS_2 drives the hole transfer from MoS_2 to WS_2 layer within 98 fs. The lifetime is obtained by exponential fitting (red dashed line in Fig. 10(d)) of the hole-transfer dynamics (black line

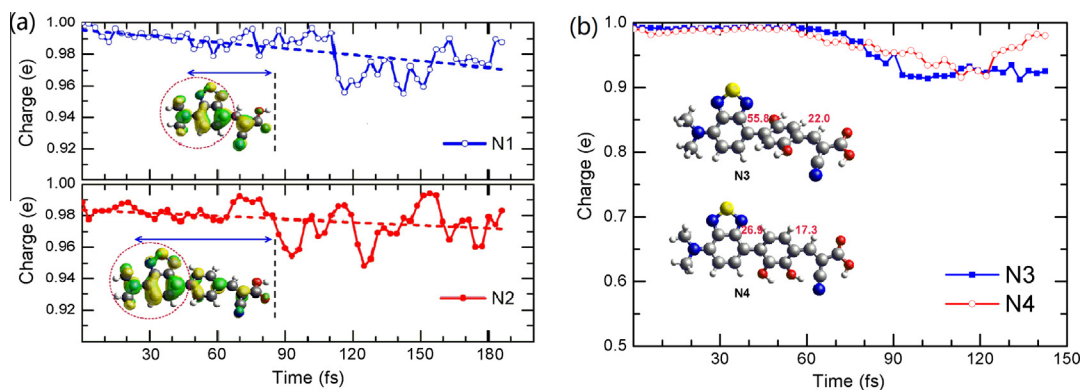


Fig. 8. (a) Fraction of electrons transferred from the TiO₂ semiconductor substrate to the organic dyes N1 and N2 after excitation at the organic dye-TiO₂ interface. Dashed lines are results fitted by a linear decaying dynamics. The two insets show back electron transfer distances from the semiconductor TiO₂ to the sensitizers. (b) Fraction of electrons transferred from the TiO₂ semiconductor substrate to the organic dyes N3 and N4 after excitation at the organic dye-TiO₂ interface. Insets are chemical structures of N3 and N4. Dyes N3 and N4 are isomers with different dihedral angles between the donor moiety and the bridging unit (shown by numbers therein).

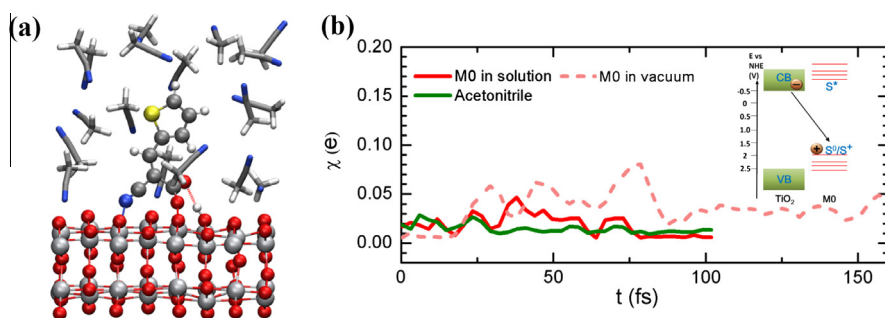


Fig. 9. (a) Schematic diagram of cyanocrylic ligand M0 dye adsorbed onto a 1 × 4 anatase slab, surrounded by acetonitrile solvent molecules. Molecules presented as sticks are acetonitrile. Color scheme: Ti – light gray, O – red, C – dark gray, N – blue, S – gold, H – white. (b) Photo-excited electron distribution on the M0 molecule (red) and solvent molecules (green) after injected into the TiO₂ CB at the organic dye/TiO₂/electrolyte heterointerface. Solid lines indicate results in solvent, while dashed lines correspond to results in vacuum. The inset shows the schematic diagram for recombination between the photo-excited electrons in TiO₂ conduction band and the holes in M0 dye. (For interpretation of the references to color in this figure legend, the reader is referred to the web version of this article.)

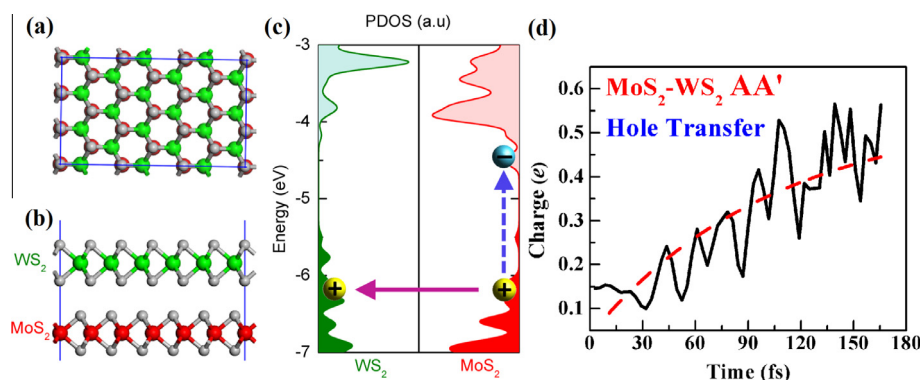


Fig. 10. (a) Top and (b) side views of MoS₂-WS₂ AA' stacking heterostructure. (c) Calculated projected density of states on WS₂ and MoS₂, respectively. (d) Hole transfer dynamics from MoS₂ layer to WS₂. At $t = 0$ fs, one electron is promoted from valence band minimum (VBM) of MoS₂ to its conduction band maximum (CBM) to simulate the initial photo-excited state.

in Fig. 10(d)), which is in considerable agreement with the experimental data (50 fs) [59].

4. Conclusion

We present an efficient real-time TDDFT approach for large-scale accurate simulations of excited state dynamics. By employing a local basis-set presentation, we are able to simulate systems of large size with affordable computation cost while maintaining

relatively high accuracy. We show several quintessential examples, such as the photo-absorption property of dye-sensitized TiO₂ nanowire, electron injection and charge recombination process in DSC, solvent effects in interface electronic dynamics in DSC, and hole-transfer dynamics between MoS₂/WS₂ interlayer. Our method is demonstrated to have superiority over other traditional methods such as trajectory surface hopping in dealing with non-adiabatic dynamics and interesting characteristics of excited states of complex systems involving massive numbers of electrons and nuclei beyond the Born–Oppenheimer approximation.

Acknowledgement

We acknowledge financial supports from MOST (2012CB921403) and NSFC (grants 11222431 and 11074287).

References

- [1] Andrew D. Liehr, *Ann. Phys.* 1 (1957) 221.
- [2] S. Bludman, P.B. Daitch, *Phys. Rev.* 95 (1954) 823.
- [3] George A. Fisk, Bernard Kirtman, *J. Chem. Phys.* 41 (1964) 3516.
- [4] Norah V. Cohan, Hendrik F. Hamerka, *J. Chem. Phys.* 45 (1966) 4392.
- [5] M.H. Beck, A. Jäckle, G.A. Worth, H.D. Meyer, *Phys. Rep.* 324 (2000) 1.
- [6] T.-S. Ho, K. Wang, S.-I. Chu, *Phys. Rev. A* 33 (1986) 1798.
- [7] K.H. Hughes, S.M. Parry, G. Parlant, I. Burghardt, *J. Phys. Chem. A* 111 (2007) 10269.
- [8] K. Wang, S.-I. Chu, *J. Chem. Phys.* 86 (1987) 3225.
- [9] J.C. Tully, R.K. Preston, *J. Chem. Phys.* 55 (1971) 562.
- [10] S.H. Schiffer, J.C. Tully, *J. Chem. Phys.* 101 (1994) 4657.
- [11] J.R. Krenos, R.K. Preston, R. Wolfgang, J.C. Tully, *J. Chem. Phys.* 60 (1974) 1634.
- [12] J.C. Tully, G.H. Gilmer, M. Shugard, *J. Chem. Phys.* 71 (1979) 1630.
- [13] D.A. Deckert, D. Dürr, P. Pickl, *J. Phys. Chem. A* 111 (2007) 10325.
- [14] Yair Goldfarb, Ilan Degani, David J. Tannor, *J. Chem. Phys.* 125 (2006) 231103.
- [15] E. Gindensperger, C. Meier, J.A. Beswick, *J. Chem. Phys.* 113 (2000) 9369.
- [16] E. Vigezzi, A. Winther, *Ann. Phys.* 192 (1989) 432.
- [17] Z.H. Huang, T.E. Feuchtwang, P.H. Cutler, E. Kazes, *Phys. Rev. A* 41 (1990) 32.
- [18] S. Takada, H. Nakamura, *J. Chem. Phys.* 100 (1994) 98.
- [19] J. Vaníček, *Phys. Rev. E* 70 (2004) 055201.
- [20] J. Vaníček, *Phys. Rev. E* 73 (2006) 046204.
- [21] B.Q. Li, C. Mollica, J. Vaníček, *J. Chem. Phys.* 131 (2009) 041101.
- [22] F.D. dos Aidos, *Phys. Lett. B* 275 (1992) 243.
- [23] C.V. Sukumar, D.M. Brink, *Nucl. Phys. A* 587 (1995) 413.
- [24] H.-D. Meyera, W.H. Miller, *J. Chem. Phys.* 70 (1979) 3214.
- [25] P.V. Parandekar, J.C. Tully, *J. Chem. Phys.* 122 (2005) 094102.
- [26] I. Tavernelli, U.F. Röhrig, U. Rothlisberger, *Mol. Phys.* 103 (2005) 963981.
- [27] S. Meng, E. Kaxiras, *J. Chem. Phys.* 129 (2008) 054110.
- [28] S. Meng, E. Kaxiras, *Biophys. J.* 95 (2008) 4396.
- [29] S. Meng, J. Ren, E. Kaxiras, *Nano Lett.* 8 (2008) 3266.
- [30] S. Meng, E. Kaxiras, *Nano Lett.* 10 (2010) 1238.
- [31] Y. Jiao, F. Zhang, M. Grätzel, S. Meng, *Adv. Funct. Mater.* 23 (2013) 424.
- [32] W. Ma, Y. Jiao, S. Meng, *J. Phys. Chem. C* 118 (2014) 16447.
- [33] A. Tsolakidis, D. Sanchez-Portal, R.M. Martin, *Phys. Rev. B* 66 (2002) 235416.
- [34] A. Tsolakidis, E. Kaxiras, *J. Phys. Chem. A* 109 (2005) 2373.
- [35] M. Hack, D. Truhlar, *J. Phys. Chem. A* 104 (2010) 7917.
- [36] P.V. Parandekar, J.C. Tully, *J. Chem. Theory Comput.* 2 (2006) 229.
- [37] J.C. Tully, *Faraday Discuss.* 110 (1998) 407.
- [38] E. Runge, E.K.U. Gross, *Phys. Rev. Lett.* 52 (1984) 997.
- [39] M. Spiegelman, R.F. Katz, *Geosystems* 7 (2006).
- [40] Z. Li, X. Zhang, G. Lu, *J. Phys. Chem. C* 116 (2012) 9845.
- [41] Z. Li, X. Zhang, G. Lu, *J. Phys. Chem. B* 114 (2010) 17077.
- [42] M. Barbatti, *Wiley Interdiscipl. Rev.: Comput. Mol. Sci.* 1 (2011) 620.
- [43] W. Ma, Y. Jiao, S. Meng, *Phys. Chem. Chem. Phys.* 15 (2013) 17187.
- [44] S. Haid, M. Marszalek, A. Mishra, M. Wielopolski, J. Teuscher, J.-E. Moser, R. Humphry-Baker, S.M. Zakeeruddin, M. Grätzel, P. Bäuerle, *Adv. Funct. Mater.* 22 (2012) 1291.
- [45] N.J. Cherepy, G.P. Smestad, M. Gratzel, J.Z. Zhang, *J. Phys. Chem. B* 101 (1997) 9342.
- [46] N. Kollias, R.M. Sayre, L. Zeise, M.R. Chedekel, *J. Photochem. Photobiol. B* 9 (1991) 135.
- [47] B.L. Seagle, E.M. Gasyna, W.F. Mieler, J.R. Norris, *Proc. Natl. Acad. Sci.* 103 (2006) 16644.
- [48] P. Meredith, T. Sarna, *Pigment Cell Res.* 19 (2006) 572.
- [49] P. Meredith, J. Riesz, *Photochem. Photobiol.* 79 (2004) 211.
- [50] J.B. Nofsinger, S.E. Forest, J.D. Simon, *J. Phys. Chem.* 103 (1999) 11428.
- [51] J.B. Nofsinger, J.D. Simon, *Photochem. Photobiol.* 74 (2001) 31.
- [52] E. Dadachova, R.A. Bryan, X. Huang, T. Moadel, A.D. Schweitzer, P. Aisen, J.D. Nosanchuk, A. Casadevall, *PLoS ONE* 2 (2007) e457.
- [53] C. Tanner, C. Manca, S. Leutwyler, *Science* 302 (2003) 1736.
- [54] W. Ma, F. Zhang, S. Meng, *Chin. Phys. B* 23 (2014) 086801.
- [55] A.K. Geim, I.V. Grigorieva, *Nature* 499 (2013) 419.
- [56] H. Lim, S.I. Yoon, G. Kim, A.R. Jang, H.S. Shin, *Chem. Mater.* 26 (2014) 4891.
- [57] M. Bernardi, M. Palummo, J.C. Grossman, *Nano Lett.* 13 (2013) 3664.
- [58] P. Rivera, J.R. Schaibley, A.M. Jones, J.S. Ross, S. Wu, G. Aivazian, P. Klement, K. Seyler, G. Clark, N.J. Ghimire, J. Yan, D.G. Mandrus, W. Yao, X. Xu, *Nat. Commun.* 6 (2015) 6242.
- [59] X. Hong, J. Kim, S.F. Shi, Y. Zhang, C. Jin, Y. Sun, S. Tongay, J. Wu, F. Wang, *Nat. Nanotechnol.* 9 (2014) 682.